Search for gravitational waves from low mass binary coalescences in the first year of LIGO's S5 data

B. P. Abbott,[17] R. Abbott,[17] R. Adhikari,[17] P. Ajith,[2] B. Allen,[2,60] G. Allen,[35] R. S. Amin,[21] S. B. Anderson,[17] W. G. Anderson,[60] M. A. Arain,[47] M. Araya,[17] H. Armandula,[17] P. Armor,[60] Y. Aso,[17] S. Aston,[46] P. Aufmuth,[16] C. Aulbert,[2] S. Babak,[1] P. Baker,[24] S. Ballmer,[17] C. Barker,[18] D. Barker,[18] B. Barr,[48] P. Barriga,[59] L. Barsotti,[20] M. A. Barton,[17] I. Bartos,[10] R. Bassiri,[48] M. Bastarrika,[48] B. Behnke,[1] M. Benacquista,[42] J. Betzwieser,[17] P. T. Beyersdorf,[31] I. A. Bilenko,[25] G. Billingsley,[17] R. Biswas,[60] E. Black,[17] J. K. Blackburn,[17] L. Blackburn,[20] D. Blair,[59] B. Bland,[18] T. P. Bodiya,[20] L. Bogue,[19] R. Bork,[17] V. Boschi,[17] S. Bose,[61] P. R. Brady,[60] V. B. Braginsky,[25] J. E. Brau,[53] D. O. Bridges,[19] M. Brinkmann,[2] A. F. Brooks,[17] D. A. Brown,[36] A. Brummit,[30] G. Brunet,[20] A. Bullington,[35] A. Buonanno,[49] O. Burmeister,[2] R. L. Byer,[35] L. Cadonati,[50] J. B. Camp,[26] J. Cannizzo,[26] K. C. Cannon,[17] J. Cao,[20] C. D. Capano,[36] L. Cardenas,[17] S. Caride,[51] G. Castaldi,[56] S. Caudill,[21] M. Cavaglià,[39] C. Cepeda,[17] T. Chalermsongsak,[17] E. Chalkley,[48] P. Charlton,[9] S. Chatterji,[17] S. Chelkowski,[46] Y. Chen,[1,6] N. Christensen,[8] C. T. Y. Chung,[38] D. Clark,[35] J. Clark,[7] J. H. Clayton,[60] T. Cokelaer,[7] C. N. Colacino,[12] R. Conte,[55] D. Cook,[18] T. R. C. Corbitt,[20] N. Cornish,[24] D. Coward,[59] D. C. Coyne,[17] J. D. E. Creighton,[60] T. D. Creighton,[42] A. M. Cruise,[46] R. M. Culter,[46] A. Cumming,[48] L. Cunningham,[48] S. L. Danilishin,[25] K. Danzmann,[2,16] B. Daudert,[17] G. Davies,[7] E. J. Daw,[40] D. DeBra,[35] J. Degallaix,[2] V. Dergachev,[51] S. Desai,[37] R. DeSalvo,[17] S. Dhurandhar,[15] M. Díaz,[42] A. Dietz,[7] F. Donovan,[20] K. L. Dooley,[47] E. E. Doomes,[34] R. W. P. Drever,[5] J. Dueck,[2] I. Duke,[20] J. -C. Dumas,[59] J. G. Dwyer,[10] C. Echols,[17] M. Edgar,[48] A. Effler,[18] P. Ehrens,[17] G. Ely,[8] E. Espinoza,[17] T. Etzel,[17] M. Evans,[20] T. Evans,[19] S. Fairhurst,[7] Y. Faltas,[47] Y. Fan,[59] D. Fazi,[17] H. Fehrmann,[2] L. S. Finn,[37] K. Flasch,[60] S. Foley,[20] C. Forrest,[54] N. Fotopoulos,[60] A. Franzen,[16] M. Frede,[2] M. Frei,[41] Z. Frei,[12] A. Freise,[46] R. Frey,[53] T. Fricke,[19] P. Fritschel,[20] V. V. Frolov,[19] M. Fyffe,[19] V. Galdi,[56] J. A. Garofoli,[36] I. Gholami,[1] J. A. Giaime,[21,19] S. Giampanis,[2] K. D. Giardina,[19] K. Goda,[20] E. Goetz,[51] L. M. Goggin,[60] G. González,[21] M. L. Gorodetsky,[25] S. Goßler,[2] R. Gouaty,[21] A. Grant,[48] S. Gras,[59] C. Gray,[18] M. Gray,[4] R. J. S. Greenhalgh,[30] A. M. Gretarsson,[11] F. Grimaldi,[20] R. Grosso,[42] H. Grote,[2] S. Grunewald,[1] M. Guenther,[18] E. K. Gustafson,[17] R. Gustafson,[51] B. Hage,[16] J. M. Hallam,[46] D. Hammer,[60] G. D. Hammond,[48] C. Hanna,[17] J. Hanson,[19] J. Harms,[52] G. M. Harry,[20] I. W. Harry,[7] E. D. Harstad,[53] K. Haughian,[48] K. Hayama,[42] J. Heefner,[17] I. S. Heng,[48] A. Heptonstall,[17] M. Hewitson,[2] S. Hild,[46] E. Hirose,[36] D. Hoak,[19] K. A. Hodge,[17] K. Holt,[19] D. J. Hosken,[45] J. Hough,[48] D. Hoyland,[59] B. Hughey,[20] S. H. Huttner,[48] D. R. Ingram,[18] T. Isogai,[8] M. Ito,[53] A. Ivanov,[17] B. Johnson,[18] W. W. Johnson,[21] D. I. Jones,[57] G. Jones,[7] R. Jones,[48] L. Ju,[59] P. Kalmus,[17] V. Kalogera,[28] S. Kandhasamy,[52] J. Kanner,[49] D. Kasprzyk,[46] E. Katsavounidis,[20] K. Kawabe,[18] S. Kawamura,[27] F. Kawazoe,[2] W. Kells,[17] D. G. Keppel,[17] A. Khalaidovski,[2] F. Y. Khalili,[25] R. Khan,[10] E. Khazanov,[14] P. King,[17] J. S. Kissel,[21] S. Klimenko,[47] K. Kokeyama,[27] V. Kondrashov,[17] R. Kopparapu,[37] S. Koranda,[60] D. Kozak,[17] B. Krishnan,[1] R. Kumar,[48] P. Kwee,[16] V. Laljani,[5] P. K. Lam,[4] M. Landry,[18] B. Lantz,[35] A. Lazzarini,[17] H. Lei,[42] M. Lei,[17] N. Leindecker,[35] I. Leonor,[53] C. Li,[6] H. Lin,[47] P. E. Lindquist,[17] T. B. Littenberg,[24] N. A. Lockerbie,[58] D. Lodhia,[46] M. Longo,[56] M. Lormand,[19] P. Lu,[35] M. Lubinski,[18] A. Lucianetti,[47] H. Lück,[2,16] A. Lundgren,[36] B. Machenschalk,[1] M. MacInnis,[20] M. Mageswaran,[17] K. Mailand,[17] I. Mandel,[28] V. Mandic,[52] S. Márka,[10] Z. Márka,[10] A. Markosyan,[35] J. Markowitz,[20] E. Maros,[17] I. W. Martin,[48] R. M. Martin,[47] J. N. Marx,[17] K. Mason,[20] F. Matichard,[21] L. Matone,[10] R. A. Matzner,[41] N. Mavalvala,[20] R. McCarthy,[18] D. E. McClelland,[4] S. C. McGuire,[34] M. McHugh,[23] G. McIntyre,[17] D. J. A. McKechan,[7] K. McKenzie,[4] M. Mehmet,[2] A. Melatos,[38] A. C. Melissinos,[54] D. F. Menéndez,[37] G. Mendell,[18] R. A. Mercer,[60] S. Meshkov,[17] C. Messenger,[2] M. S. Meyer,[19] J. Miller,[48] J. Minelli,[37] Y. Mino,[6] V. P. Mitrofanov,[25] G. Mitselmakher,[47] R. Mittleman,[20] O. Miyakawa,[17] B. Moe,[60] S. D. Mohanty,[42] S. R. P. Mohapatra,[50] G. Moreno,[18] T. Morioka,[27] K. Mors,[2] K. Mossavi,[2] C. MowLowry,[4] G. Mueller,[47] H. Müller-Ebhardt,[2] D. Muhammad,[19] S. Mukherjee,[42] H. Mukhopadhyay,[15] A. Mullavey,[4] J. Munch,[45] P. G. Murray,[48] E. Myers,[18] J. Myers,[18] T. Nash,[17] J. Nelson,[48] G. Newton,[48] A. Nishizawa,[27] K. Numata,[26] J. O'Dell,[30] B. O'Reilly,[19] R. O'Shaughnessy,[37] E. Ochsner,[49] G. H. Ogin,[17] D. J. Ottaway,[45] R. S. Ottens,[47] H. Overmier,[19] B. J. Owen,[37] Y. Pan,[49] C. Pankow,[47] M. A. Papa,[1,60] V. Parameshwaraiah,[18] P. Patel,[17] M. Pedraza,[17] S. Penn,[13] A. Perreca,[46] V. Pierro,[56] I. M. Pinto,[56] M. Pitkin,[48] H. J. Pletsch,[2] M. V. Plissi,[48] F. Postiglione,[55] M. Principe,[56] R. Prix,[2] L. Prokhorov,[25] O. Punken,[2] V. Quetschke,[47] F. J. Raab,[18] D. S. Rabeling,[4] H. Radkins,[18] P. Raffai,[12] Z. Raics,[10] N. Rainer,[2] M. Rakhmanov,[42] V. Raymond,[28] C. M. Reed,[18] T. Reed,[22] H. Rehbein,[2] S. Reid,[48] D. H. Reitze,[47] R. Riesen,[19] K. Riles,[51] B. Rivera,[18] P. Roberts,[3] N. A. Robertson,[17,48] C. Robinson,[7] E. L. Robinson,[1] S. Roddy,[19] C. Röver,[2] J. Rollins,[10] J. D. Romano,[42] J. H. Romie,[19] S. Rowan,[48] A. Rüdiger,[2] P. Russell,[17] K. Ryan,[18] S. Sakata,[27] L. Sancho de la Jordana,[44] V. Sandberg,[18] V. Sannibale,[17] L. Santamaría,[1] S. Saraf,[32] P. Sarin,[20] B. S. Sathyaprakash,[7] S. Sato,[27] M. Satterthwaite,[4]

P. R. Saulson,[36] R. Savage,[18] P. Savov,[6] M. Scanlan,[22] R. Schilling,[2] R. Schnabel,[2] R. Schofield,[53] B. Schulz,[2] B. F. Schutz,[1,7] P. Schwinberg,[18] J. Scott,[48] S. M. Scott,[4] A. C. Searle,[17] B. Sears,[17] F. Seifert,[2] D. Sellers,[19] A. S. Sengupta,[17] A. Sergeev,[14] B. Shapiro,[20] P. Shawhan,[49] D. H. Shoemaker,[20] A. Sibley,[19] X. Siemens,[60] D. Sigg,[18] S. Sinha,[35] A. M. Sintes,[44] B. J. J. Slagmolen,[4] J. Slutsky,[21] J. R. Smith,[36] M. R. Smith,[17] N. D. Smith,[20] K. Somiya,[6] B. Sorazu,[48] A. Stein,[20] L. C. Stein,[20] S. Steplewski,[61] A. Stochino,[17] R. Stone,[42] K. A. Strain,[48] S. Strigin,[25] A. Stroeer,[26] A. L. Stuver,[19] T. Z. Summerscales,[3] K. -X. Sun,[35] M. Sung,[21] P. J. Sutton,[7] G. P. Szokoly,[12] D. Talukder,[61] L. Tang,[42] D. B. Tanner,[47] S. P. Tarabrin,[25] J. R. Taylor,[2] R. Taylor,[17] J. Thacker,[19] K. A. Thorne,[19] K. S. Thorne,[6] A. Thüring,[16] K. V. Tokmakov,[48] C. Torres,[19] C. Torrie,[17] G. Traylor,[19] M. Trias,[44] D. Ugolini,[43] J. Ulmen,[35] K. Urbanek,[35] H. Vahlbruch,[16] M. Vallisneri,[6] C. Van Den Broeck,[7] M. V. van der Sluys,[28] A. A. van Veggel,[48] S. Vass,[17] R. Vaulin,[60] A. Vecchio,[46] J. Veitch,[46] P. Veitch,[45] C. Veltkamp,[2] A. Villar,[17] C. Vorvick,[18] S. P. Vyachanin,[25] S. J. Waldman,[20] L. Wallace,[17] R. L. Ward,[17] A. Weidner,[2] M. Weinert,[2] A. J. Weinstein,[17] R. Weiss,[20] L. Wen,[6,59] S. Wen,[21] K. Wette,[4] J. T. Whelan,[1,29] S. E. Whitcomb,[17] B. F. Whiting,[47] C. Wilkinson,[18] P. A. Willems,[17] H. R. Williams,[37] L. Williams,[47] B. Willke,[2,16] I. Wilmut,[30] L. Winkelmann,[2] W. Winkler,[2] C. C. Wipf,[20] A. G. Wiseman,[60] G. Woan,[48] R. Wooley,[19] J. Worden,[18] W. Wu,[47] I. Yakushin,[19] H. Yamamoto,[17] Z. Yan,[59] S. Yoshida,[33] M. Zanolin,[11] J. Zhang,[51] L. Zhang,[17] C. Zhao,[59] N. Zotov,[22] M. E. Zucker,[20] H. zur Mühlen,[16] and J. Zweizig[17]

(LIGO Scientific Collaboration)[*]

[1]*Albert-Einstein-Institut, Max-Planck-Institut für Gravitationsphysik, D-14476 Golm, Germany*
[2]*Albert-Einstein-Institut, Max-Planck-Institut für Gravitationsphysik, D-30167 Hannover, Germany*
[3]*Andrews University, Berrien Springs, Michigan 49104, USA*
[4]*Australian National University, Canberra, 0200, Australia*
[5]*California Institute of Technology, Pasadena, California 91125, USA*
[6]*Caltech-CaRT, Pasadena, California 91125, USA*
[7]*Cardiff University, Cardiff, CF24 3AA, United Kingdom*
[8]*Carleton College, Northfield, Minnesota 55057, USA*
[9]*Charles Sturt University, Wagga Wagga, NSW 2678, Australia*
[10]*Columbia University, New York, New York 10027, USA*
[11]*Embry-Riddle Aeronautical University, Prescott, Arizona 86301 USA*
[12]*Eötvös University, ELTE 1053 Budapest, Hungary*
[13]*Hobart and William Smith Colleges, Geneva, New York 14456, USA*
[14]*Institute of Applied Physics, Nizhny Novgorod, 603950, Russia*
[15]*Inter-University Centre for Astronomy and Astrophysics, Pune–411007, India*
[16]*Leibniz Universität Hannover, D-30167 Hannover, Germany*
[17]*LIGO–California Institute of Technology, Pasadena, California 91125, USA*
[18]*LIGO–Hanford Observatory, Richland, Washington 99352, USA*
[19]*LIGO–Livingston Observatory, Livingston, Louisiana 70754, USA*
[20]*LIGO–Massachusetts Institute of Technology, Cambridge, Massachusetts 02139, USA*
[21]*Louisiana State University, Baton Rouge, Louisiana 70803, USA*
[22]*Louisiana Tech University, Ruston, Louisiana 71272, USA*
[23]*Loyola University, New Orleans, Louisiana 70118, USA*
[24]*Montana State University, Bozeman, Montana 59717, USA*
[25]*Moscow State University, Moscow, 119992, Russia*
[26]*NASA/Goddard Space Flight Center, Greenbelt, Maryland 20771, USA*
[27]*National Astronomical Observatory of Japan, Tokyo 181-8588, Japan*
[28]*Northwestern University, Evanston, Illinois 60208, USA*
[29]*Rochester Institute of Technology, Rochester, New York 14623, USA*
[30]*Rutherford Appleton Laboratory, HSIC, Chilton, Didcot, Oxon OX11 0QX United Kingdom*
[31]*San Jose State University, San Jose, California 95192, USA*
[32]*Sonoma State University, Rohnert Park, California 94928, USA*
[33]*Southeastern Louisiana University, Hammond, Louisiana 70402, USA*
[34]*Southern University and A&M College, Baton Rouge, Louisiana 70813, USA*
[35]*Stanford University, Stanford, California 94305, USA*
[36]*Syracuse University, Syracuse, New York 13244, USA*
[37]*The Pennsylvania State University, University Park, Pennsylvania 16802, USA*
[38]*The University of Melbourne, Parkville VIC 3010, Australia*
[39]*The University of Mississippi, University, Mississippi 38677, USA*

^{40}*The University of Sheffield, Sheffield S10 2TN, United Kingdom*
^{41}*The University of Texas at Austin, Austin, Texas 78712, USA*
^{42}*The University of Texas at Brownsville and Texas Southmost College, Brownsville, Texas 78520, USA*
^{43}*Trinity University, San Antonio, Texas 78212, USA*
^{44}*Universitat de les Illes Balears, E-07122 Palma de Mallorca, Spain*
^{45}*University of Adelaide, Adelaide, SA 5005, Australia*
^{46}*University of Birmingham, Birmingham, B15 2TT, United Kingdom*
^{47}*University of Florida, Gainesville, Florida 32611, USA*
^{48}*University of Glasgow, Glasgow, G12 8QQ, United Kingdom*
^{49}*University of Maryland, College Park, Maryland 20742 USA*
^{50}*University of Massachusetts–Amherst, Amherst, Massachusetts 01003, USA*
^{51}*University of Michigan, Ann Arbor, Michigan 48109, USA*
^{52}*University of Minnesota, Minneapolis, Minnesota 55455, USA*
^{53}*University of Oregon, Eugene, Oregon 97403, USA*
^{54}*University of Rochester, Rochester, New York 14627, USA*
^{55}*University of Salerno, 84084 Fisciano (Salerno), Italy*
^{56}*University of Sannio at Benevento, I-82100 Benevento, Italy*
^{57}*University of Southampton, Southampton, SO17 1BJ, United Kingdom*
^{58}*University of Strathclyde, Glasgow, G1 1XQ, United Kingdom*
^{59}*University of Western Australia, Crawley, WA 6009, Australia*
^{60}*University of Wisconsin–Milwaukee, Milwaukee, Wisconsin 53201, USA*
^{61}*Washington State University, Pullman, Washington 99164, USA*

We have searched for gravitational waves from coalescing low mass compact binary systems with a total mass between $2M_\odot$ and $35M_\odot$ and a minimum component mass of $1M_\odot$ using data from the first year of the fifth science run of the three LIGO detectors, operating at design sensitivity. Depending on the mass, we are sensitive to coalescences as far as 150 Mpc from the Earth. No gravitational-wave signals were observed above the expected background. Assuming a population of compact binary objects with a Gaussian mass distribution representing binary neutron star systems, black hole–neutron star binary systems, and binary black hole systems, we calculate the 90% confidence upper limit on the rate of coalescences to be 3.9×10^{-2} yr$^{-1}L_{10}^{-1}$, 1.1×10^{-2} yr$^{-1}L_{10}^{-1}$, and 2.5×10^{-3} yr$^{-1}L_{10}^{-1}$, respectively, where L_{10} is 10^{10} times the blue solar luminosity. We also set improved upper limits on the rate of compact binary coalescences per unit blue-light luminosity, as a function of mass.

I. INTRODUCTION

Among the most promising candidates for the first detection of gravitational waves (GW) are signals from compact binary coalescences (CBC), which include binary neutron stars (BNS), binary black holes (BBH), and black hole–neutron star binaries (BHNS). The inspiral waveforms generated by these systems can be reliably predicted using post-Newtonian (PN) perturbation theory, until the last fraction of a second prior to merger. These waveforms can be used in matched filtering of noisy data from gravitational-wave detectors to identify GW candidate events.

Astrophysical estimates for CBC rates depend on a number of assumptions and unknown model parameters, and are still uncertain at present. In the simplest models, the coalescence rates should be proportional to the stellar birth rate in nearby spiral galaxies, which can be estimated from their blue luminosity [1]; we therefore express the coalescence rates per unit L_{10}, where L_{10} is 10^{10} times the blue solar luminosity (the Milky Way contains $\sim 1.7L_{10}$ [2]). The most confident BNS rate predictions are based on extrapolations from observed binary pulsars in our Galaxy; these yield realistic BNS rates of 5×10^{-5} yr$^{-1}L_{10}^{-1}$, although rates could plausibly be as high as 5×10^{-4} yr$^{-1}L_{10}^{-1}$ [3,4]. Predictions for BBH and BHNS rates are based on population synthesis models constrained by these and other observations. Realistic rate estimates are 2×10^{-6} yr$^{-1}L_{10}^{-1}$ for BHNS [5] and 4×10^{-7} yr$^{-1}L_{10}^{-1}$ for BBH [6]; both BHNS and BBH rates could plausibly be as high as 6×10^{-5} yr$^{-1}L_{10}^{-1}$ [5,6].

The Laser Interferometer Gravitational-wave Observatory (LIGO) detectors achieved design sensitivity in 2005, and completed a two-year-long science run (S5) in November 2007. Results from searches for GW from CBC by the LIGO Scientific Collaboration (LSC) using data from previous science runs with ever-increasing sensitivity are reported in Refs. [7–11].

This paper summarizes the search for GW signals from CBC with component masses greater than or equal to 1

solar mass ($M_\odot$) and total mass ranging from $2M_\odot$ to $35M_\odot$, using the first year of data from LIGO's S5 run, between November 4, 2005 and November 14, 2006. During this time, the LIGO detectors were sensitive to signals from CBC with horizon distances (Table II) of 30 Mpc for BNS (25 seconds in the LIGO detection band) and 150 Mpc for systems with a total mass of $\sim 28M_\odot$ (0.5 seconds in the LIGO band). Subsequent papers will report the results of similar searches using the data from the second year (during which time the Virgo detector was in observational mode), searches for higher mass systems (between $25M_\odot$ and $100M_\odot$), and specialized searches targeting particular subsets of signals.

The component objects of true astrophysical compact binaries will, in general, have some angular momentum, for which PN waveforms that incorporate nonzero values for the spin parameters are available [12,13]. However, for most of the parameter space, the effect of spin on the waveforms is small, and the signals can be captured using nonspinning waveform templates (Appendix I) with only a small loss in the signal-to-noise ratio (SNR); this is the approach taken in the search described here. In some regions of parameter space, the effect of spin is larger, and dedicated searches [13–16] may be more effective. The LSC continues to develop more effective methods for searching for signals with strong modulations due to spin.

The rest of this paper is organized as follows. Section II summarizes the search pipeline that was employed. Section III describes the output of the search: detection candidate events which are examined and rejected using a detection confidence procedure. Section IV describes the evaluation of our detection efficiency using simulated GW signals injected into the detectors' data streams. Section V discusses the upper limit calculation that was performed, and the resulting upper limits on CBC rates neglecting the spin of the coalescing objects. Section VI discusses how our sensitivity is affected when spin is included. Finally, Sec. VII presents the conclusions, followed by several appendixes on certain technical aspects of the search.

II. THE DATA ANALYSIS PIPELINE

The pipeline used for this analysis has been described in previous documents [17–20], and was used to search for BNS in LIGO's third and fourth science runs [11]. The main aspects of the pipeline and new features used here are detailed below.

The data analysis proceeds as follows. The gravitational-wave strain data are recorded from each of the three LIGO detectors: the H1 and H2 detectors at LIGO Hanford Observatory (LHO) and the L1 detector at LIGO Livingston Observatory (LLO). These data are matched filtered through banks of templates that model the expected signal from a binary coalescence of two compact massive objects with masses m_1 and m_2, resulting in triggers that pass a preset SNR threshold. We search for coincident triggers in time and template masses, between two or three detectors. We subject these coincident triggers to several tests to suppress noise fluctuations (including the χ^2 test described in [21]), and rank-order the remaining coincident triggers according to their inconsistency with the background.

We estimate the background from accidental coincidences by looking at time-shifted coincident triggers, as detailed in Sec. II D. Coincident triggers that are not consistent with the estimated background are followed up with many additional consistency checks, designed to identify strong but rare noise fluctuations. We estimate our sensitivity to GW signals through injections of simulated waveforms into the LIGO data stream which are analyzed identically to the data.

A. Template bank

The templates used for this search are waveforms from nonspinning compact binaries calculated in the frequency domain using the stationary-phase approximation (SPA) [22–24]. The waveforms are calculated to Newtonian order in amplitude and to second PN order in phase, and they extend until the Schwarzschild innermost stable circular orbit (ISCO). The templates for this single search cover a larger binary mass region than in previous searches [11], with a total mass (M) of $2M_\odot < M < 35M_\odot$ and a minimum component mass of $1M_\odot$. The templates are placed with a hexagonal spacing [25] such that we lose less than 3% of the SNR due to using a discrete template bank to cover the continuous parameter space spanned by the two component masses.

B. Analyzed and vetoed times

The pipeline is applied to data from the first year of the LIGO S5 run, for which more than one detector was in observation mode. This comprises 0.419 yr of triple-coincident data (H1H2L1), 0.232 yr of H1H2 coincident data, 0.037 yr of H1L1 coincident data, and 0.047 yr of H2L1 coincident data. In determining our upper limits, we exclude approximately 9.5% of the data that were used to tune the pipeline [18] (the *playground* data). We also exclude all the data when only the H1 and H2 detectors were in observation mode, because of the difficulty in determining the background from coincident noise triggers in these collocated detectors (Sec. II D). We make use of the (rather large amount of) additional information on the state of the detectors and the physical environment to define data quality (DQ) criteria (Appendix A). We use these DQ criteria to veto triggers in times when an individual detector was in observation mode where we also have reason to believe the data were contaminated by instrumental or environmental problems. We define four categories of vetoes from these DQ criteria, based on the severity of the data quality issue, and how well we under-

stand its origin, explained in Appendix A. We follow up detection candidates after successively applying each veto category (Appendix B). We exclude from the upper limit calculation times flagged with DQ vetoes in the first three categories, along with triggers recorded in those times. This results in nonvetoed, nonplayground observation times of 0.336 yr for H1H2L1, 0.020 yr for H1L1, and 0.041 yr for H2L1.

C. Coincidence test and clustering

Our analysis applies a more sophisticated coincidence test than the one used in the past. Previously, in order for triggers from different interferometers to be considered *coincident triggers*, they needed to pass a series of independent windows in time, chirp mass ($M_c = \eta^{3/5}M$), and symmetric mass ratio ($\eta = m_1 m_2/M^2$). These windows were defined independently of the parameters of the triggers (e.g. M_c, η).

We have replaced this coincidence test with the one [26] that is based on the metric used in constructing a template bank [20,27–29]. The metric contains terms necessary for measuring distances and determining coincidence in masses and time as well as the correlations between the parameters expected for real signal events in the three-dimensional parameter space. This provides improved separation between signals and background from accidental coincidence of noise triggers, compared to the above independent windows.

We have also changed the algorithm used to cluster single-detector triggers in our pipeline. Previously, the triggers were clustered by retaining the trigger with the largest SNR from all the templates over a fixed window of time. At present, we use a new method [30] to cluster triggers, analogous to the coincidence algorithm, again retaining the trigger with the largest SNR from a particular cluster.

D. Background estimation

As in the previous searches, we estimate the background due to accidental coincidences of noise triggers by repeating the analysis with the triggers from different detectors shifted in time relative to each other, forming 100 experimental trials with no true signals. We refer to these as *time-shifted coincident triggers*, as opposed to the *in-time coincident triggers* obtained without the use of time shifts.

This procedure is known to underestimate the rate of accidental coincidences of noise triggers from the H1 and H2 detectors, since they are collocated and exhibit time-correlated noise excursions. We therefore exclude H1H2 double-coincident data from the upper limit calculation. We examine only the very strongest H1H2 double-coincident detection candidates (including H1H2 coincidences that did not appear in L1), and subject them to very stringent scrutiny. There were no H1H2 candidates that survived these checks. (See Sec. III for details.)

E. Detection statistic

In this search, we employ a new detection statistic which allows us to search over a large region of parameter space without being limited by a high background false alarm rate (FAR) from a smaller subregion. In Ref. [11], coincident triggers were ranked by combined effective SNR (Appendix C). Here, instead, we use a statistic derived from the background FAR, as detailed in Appendix D. The time-shifted triggers provide an estimate of the FAR for each in-time coincident trigger. By counting the number of time-shifted triggers with an effective SNR greater than or equal to the in-time coincident triggers' effective SNR, and dividing by the total amount of time we searched for time-shifted triggers, we calculate the FAR for each in-time coincident trigger. This procedure is done separately for different regions of parameter space, with the result that the FAR as a function of effective SNR varies over the parameter space. In-time coincident triggers with the largest inverse false alarm rate (IFAR) are our best detection candidates.

III. DETECTION CANDIDATES

At the end of our pipeline we are left with a set of coincident triggers that are potential detection candidates. The cumulative distribution of events above a threshold IFAR is shown in Fig. 1. This figure shows that the loudest candidates in all three sets were consistent with the estimated background and thus were likely accidental coincidences. Thus, the search yielded no detection candidates, and we report an upper limit in Secs. V and VI.

As an exercise to prepare for future detections, we carry the loudest several events (such as the three loudest events that appear in each of the histograms in Fig. 1) through a detection checklist described in Appendix B. The methods employed in this checklist are tested against simulated GW signals and the time-shifted coincidence triggers used to estimate the background.

Even though we know our background is underestimated for H1H2 coincident triggers, we reviewed the two loudest H1H2 candidates using the detection checklist. In both of those cases, the waveforms from the two interferometers failed to match each other in detail, thus ruling them out as gravitational-wave events.

During the analysis, and prior to unblinding the nonplayground data, an error was found in the coincidence algorithm (Appendix B). This caused the coincidence requirement to be tighter than initially intended. It had a negligible effect for low mass templates, but became more significant at higher masses. However, since the coincidence threshold was selected based upon the examination of simulated signals, we decided to use this search in generating the upper limits presented here. We verified the detection candidates by rerunning the search after correcting the coincidence test. The results of the corrected
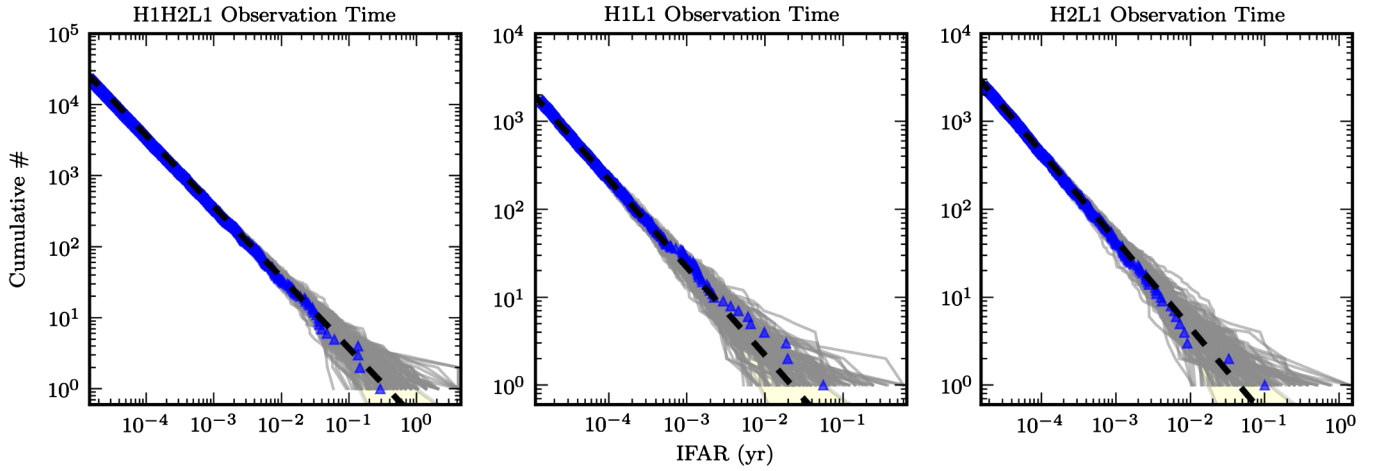
FIG. 1 (color online). The cumulative distribution of events above a threshold IFAR, for in-time coincident events, shown as blue triangles, from all coincidence categories for the observation times H1H2L1, H1L1, and H2L1, respectively. The expected background (by definition) is shown as a dashed black line. The 100 experimental trials that make up our background are also plotted individually as the solid grey lines. The shaded region denotes the $N^{1/2}$ errors.

search did not provide any plausible gravitational-wave signals.

IV. DETECTION EFFICIENCY

We evaluate our efficiency for detecting GW signals from CBC during the first year of S5 as a function of mass and of distance to the source. This is done by coherently injecting a large number of simulated signals, called software injections, into the detector data streams. Those data are then analyzed with a pipeline identical to that used to search for detection candidates. The distribution of masses, distances, sky locations, orientations, and component spins is described in Appendix E. The procedure for calculating the detection efficiency is described in Appendix F, where a software injection is considered to be detected if its IFAR exceeds that of the coincident in-

TABLE I. Detailed results from the BNS upper limit calculation. The observation time is reported after category 3 vetoes. The cumulative luminosity is the luminosity to which the search is sensitive above the loudest event for each coincidence time, and is rounded to two significant figures. The errors in this table are listed as logarithmic errors in the luminosity multiplier based on the cited sources of error.

Coincidence time	H1H2L1	H1L1	H2L1
Observation time (yr)	0.336	0.020	0.041
Cumulative luminosity (L_{10})	~250	~230	~120
Calibration error	21%	3.9%	16%
Monte Carlo error	5.4%	16%	13%
Waveform error	26%	11%	20%
Galaxy distance error	14%	13%	6.1%
Galaxy magnitude error	17%	17%	16%
Λ [Eq. (G2)]	0.30	0.41	0.72

time trigger with the highest IFAR. We find that our detection efficiencies are consistent with expectations from the detectors' noise spectra during S5.

As noted in Secs. I and II, we are using nonspinning templates to look for GW from CBC, whereas true GW signals from CBC will have some amount of spin associated with the objects. Therefore, in the next two sections, we evaluate our detection efficiency using injections of both nonspinning and spinning simulated signals.

Appendix I gives a comparison of the pipeline described above and one using phenomenological waveforms [13–16,31]. The present pipeline admits the use of the χ^2 test [21], which reduces the false alarm rate at a given SNR threshold. Because of this, when we reduce the SNR threshold of the present pipeline to find the value that gives the same false alarm rate as the phenomenological pipeline, we effectively compensate for the lost signal power associated with using nonspinning templates to search for spinning systems.

V. UPPER LIMITS NEGLECTING SPIN

In the absence of detection, we set upper limits on the rate of CBC per unit L_{10}, for several canonical binary systems and as a function of mass of the compact binary system.

For each mass range of interest, we calculate the 90% confidence level (CL) upper limit on the rate using the loudest event formalism [32,33], described in Appendix G. In the limit where the loudest event is consistent with the background, the upper limit we obtain tends toward $\mathcal{R}_{90\%} \sim 2.303/(T\mathcal{C}_L)$, where T is the total observation time (in years) and $\mathcal{C}_L$ is the cumulative luminosity (in L_{10}) to which this search is sensitive above its loudest event. We derive a Bayesian posterior distribution for the rate, as described in Ref. [33].

TABLE II.   Overview of results of the upper limit calculations summary of the search for BNS, BBH, and BHNS systems. The horizon distance is the distance at which an optimally oriented and optimally located source with the appropriate mass would produce a trigger with a SNR of 8 in the 4 km detectors and averaged over the search. The cumulative luminosity and Λ are from H1H2L1 time and are rounded to two significant figures.

System	BNS	BBH	BHNS
Component masses ($M_\odot$)	1.35/1.35	5.0/5.0	5.0/1.35
D_{horizon} (Mpc)	~30	~80	~50
Cumulative luminosity (L_{10})	250	4900	990
Λ [Eq. (G2)]	0.30	0.59	0.45
Marginalized upper limit ($\text{yr}^{-1}L_{10}^{-1}$)	3.9×10^{-2}	2.5×10^{-3}	1.1×10^{-2}

In order to evaluate the cumulative luminosity, we multiply the detection efficiency, as a function of mass and distance, by the luminosity calculated from a galaxy population [1] for the nearby universe. The cumulative luminosity is then this product integrated over distance. The cumulative luminosities associated with this search can be found in Tables I and II.

We apply the above upper limit calculation to three canonical binary masses as well as calculate the upper limit as a function of mass. Our three canonical binary masses are BNS [$m_1 = m_2 = (1.35 \pm 0.04)M_\odot$], BBH [$m_1 = m_2 = (5 \pm 1)M_\odot$], and BHNS [$m_1 = (5 \pm 1)M_\odot$, $m_2 = (1.35 \pm 0.04)M_\odot$]. We represent these systems as Gaussian distributions in component mass centered on these masses with standard deviations given above following the $\pm$ symbols.

We combine the results of this search from the three different observation times in a Bayesian manner, described in Appendix G, and the results from previous science runs [11,13] are incorporated in a similar way.

Assuming that spin is not important in these systems, we calculate upper limits on the rate of binary coalescences

using our injection families that neglect spin (Appendix E). There are a number of uncertainties which affect the upper limit, including systematic errors associated with detector calibration, simulation waveforms, Monte Carlo statistics, and galaxy catalog distances and magnitudes [19]. We marginalize over these, as described in Appendix H, and obtain upper limits on the rate of binary coalescences of

$$\mathcal{R}_{90\%,\text{BNS}} = 3.9 \times 10^{-2} \text{ yr}^{-1}L_{10}^{-1}, \qquad (1)$$

$$\mathcal{R}_{90\%,\text{BBH}} = 2.5 \times 10^{-3} \text{ yr}^{-1}L_{10}^{-1}, \qquad (2)$$

$$\mathcal{R}_{90\%,\text{BHNS}} = 1.1 \times 10^{-2} \text{ yr}^{-1}L_{10}^{-1}. \qquad (3)$$

We also calculate upper limits for two additional cases: as a function of the total mass of the binary, with a uniform distribution in the mass ratio $q = m1/m2$, and as a function of the mass of the black hole in a BHNS system, holding fixed the mass of the neutron star at $m_{\text{NS}} = 1.35M_\odot$ (Fig. 2).
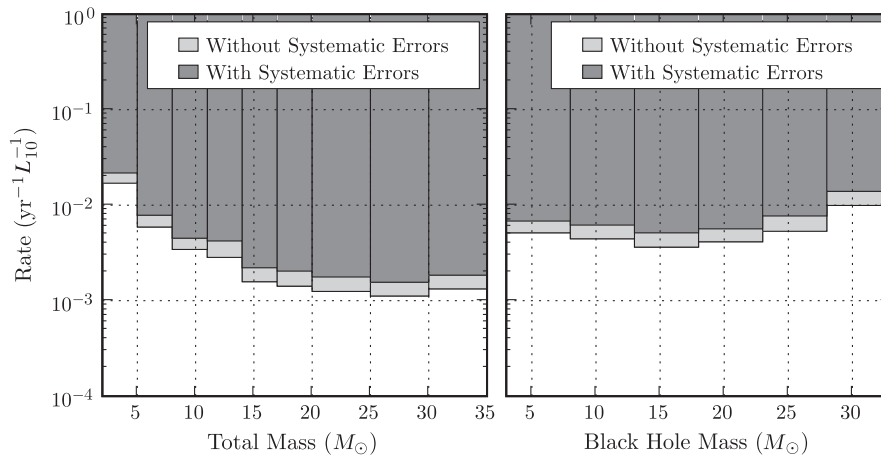

FIG. 2.   Upper limits on the binary coalescence rate per year and per L_{10} as a function of total mass of the binary system with a uniform distribution in the mass ratio (left panel) and as a function of the mass of a black hole in a BHNS system with a neutron star mass of $1.35M_\odot$ (right panel). The darker area shows the excluded region after accounting for marginalization over the estimated systematic errors. The lighter area shows the additional region that would have existed if the systematic errors had been ignored.

VI. UPPER LIMITS INCLUDING SPIN

Above, we have reported upper limits on the rate of mergers for different classes of objects using injection waveforms generated assuming nonspinning objects. We can also evaluate the upper limits using injection waveforms that take into account the effects of spinning bodies.

Since the maximum possible rotational angular momentum S for a black hole of mass m is Gm^2/c, it is useful to describe the spin of a compact object in terms of the dimensionless spin parameter $\hat{a} = (cS)/(Gm^2)$. The distribution of black hole spin magnitudes within the range $0 \leq \hat{a} \leq 1$, as well as their orientations relative to binary orbits, is not well constrained by observations. To illustrate the possible effects of BH spins on our sensitivity to BBH and BHNS signals, we provide an example calculation using a set of injections of signals simulating systems whose component objects have $\hat{a}$ uniformly distributed between 0 and 1 (Appendix E). On the other hand, assuming a canonical mass and uniform density, astrophysical observations of neutron stars show typical angular momenta corresponding to $\hat{a} \ll 1$ [34]. In addition, the spin effects are found to be weak for the frequency range of interest for LIGO [35], so the BNS upper limits in Sec. V are valid even though we have ignored the effects of spin.

Using the above injections, we obtain marginalized upper limits on the rate of binary coalescences of

$$\mathcal{R}_{90\%,\mathrm{BBH}} = 3.2 \times 10^{-3} \ \mathrm{yr}^{-1}L_{10}{}^{-1}, \tag{4}$$

$$\mathcal{R}_{90\%,\mathrm{BHNS}} = 1.4 \times 10^{-2} \ \mathrm{yr}^{-1}L_{10}{}^{-1}. \tag{5}$$

VII. CONCLUSIONS

We have searched for gravitational waves from coalescing compact binary systems with total mass ranging from $2M_\odot$ to $35M_\odot$, using data from the first year of S5 from the three initial LIGO detectors. In doing so, we have investigated the efficacy of searching for BBH signals with 2PN SPA nonspinning templates and have found them to be effective even at the relatively high total mass of $35M_\odot$. Additionally, we have found that the nonspinning templates can effectively capture spinning signals with some loss of efficiency. The result of the search was that no plausible gravitational-wave signals were observed above the background. We set upper limits on the rate of these types of events that are 2 orders of magnitude smaller than the previous observational upper limits [11,13], although they are still several orders of magnitude above the range of astrophysical estimates [3,4,6,36]. In the coming years, LIGO and other ground-based detectors will undergo significant upgrades. We expect to be able to significantly improve our sensitivity to gravitational waves from compact binary coalescences and are preparing for the first detections and studies.

APPENDIX A: DATA QUALITY CRITERIA

When analyzing data from LIGO's detectors, it is important to know the status of the detectors at different times. We define DQ flags as time intervals containing known artifacts introduced into the data by instrumental or environmental effects. We examine the correlation between triggers from an individual detector and the DQ flags. If we find a correlation larger than that expected based on the fraction of time vetoed (which we call the *dead time*), we use them as vetoes. Our understanding of the coupling between the effect that prompted the DQ flag and the resulting triggers in the pipeline is measured in part by the fraction of the DQ flags that are used to veto triggers (called the *use percentage*). We define four different categories of DQ vetoes based on the above criteria.

We categorize DQ vetoes as *category 1 vetoes* when we know of a severe problem with the data, bringing into question whether the detector was actually in observation mode. An example case for H2 is when loud vibrations were caused in the detector environment in order to test the response of the seismic isolation systems. We categorize DQ vetoes as *category 2 vetoes* when there is a known coupling between the GW channel and the auxiliary channel, the veto is correlated with triggers from the individual detector, particularly at high SNR, and when there is a use percentage of 50% or greater. An example is when any of the data channels in the length sensing and control servo reach their digital limit. We categorize DQ vetoes as *category 3 vetoes* when the coupling between the auxiliary channel and the GW channel is less established or when the use percentage is low, but we still find a strong correlation
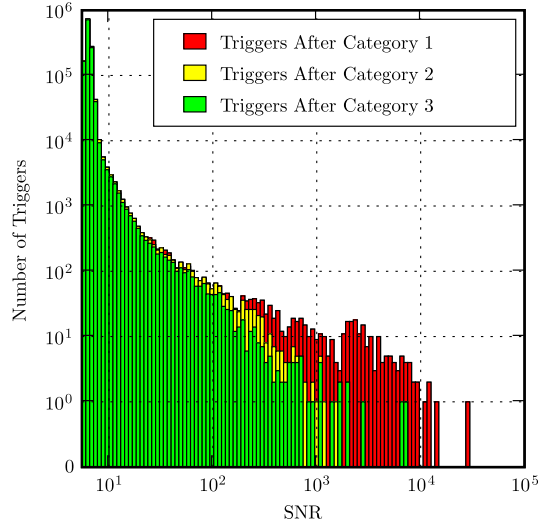
FIG. 3 (color online). Histogram of triggers for the H2 detector, clustered by the trigger with maximum SNR within 10 seconds, plotted after removing triggers occurring during times vetoed by category 1, 2, and 3 vetoes. The tail of the SNR distribution is significantly reduced by both category 2 and 3 vetoes.

between the vetoes and the triggers. An example is when the winds at the detector site are over 30 MPH. We categorize DQ vetoes as *category 4 vetoes* when the coupling between the auxiliary channel and the GW channel is not well established, when the use percentage is low, when the overall dead time is several percent or greater, or when the correlation is weak. An example is when nearby aircraft pass overhead. We compare all of these vetoes with the times of hardware injections, which measure the response of the detector to a simulated gravitational-wave signal, in order to confirm that the DQ vetoes are not sensitive to real signals in the data.

We do not analyze data vetoed by category 1 DQ vetoes. We remove triggers in times defined by category 2 and 3 DQ vetoes from the upper limit calculation. These veto categories significantly reduce the SNR of outlying triggers (Fig. 3). As an exercise, we follow up the loudest coincident triggers after each category of veto is applied, including after category 4 vetoes (see Appendix B). This allows us to investigate the action of the vetoes by a "case study" method.

APPENDIX B: FOLLOW-UP PROCEDURE FOR COINCIDENT TRIGGERS

As an exercise, we check our loudest coincident triggers with a list of tests designed to see if a statistically significant trigger is believable as a detection candidate. Reference [37] describes the tests that we perform on the trigger and the data surrounding it. At present, our standard tests include the following: We check the integrity of the data for corruption. We also check the status of the detec-

tors and the presence of any data quality flags in the surrounding data. We assess whether there could have been environmental or instrumental causes found in auxiliary channels at the time of the trigger. We check the appearance of the data at the time of the trigger in the form of SNR time series, χ^2 time series, and time-frequency spectrograms.

In addition, for any statistically significant candidate that survives the tests listed above, we plan to do the following: Assess the coherence between the signals recorded by each individual detector operating at the time of the event. Verify the robustness of the trigger against small changes in the pipeline (i.e. changes in the adjacent Fourier transform boundaries or changes in the calibration of the data). Check the robustness across pipelines by employing other search techniques to analyze the same data (i.e. CBC pipelines using different templates or algorithms designed to search for unmodeled bursts). Finally, we will check for coincidence with external searches for gamma-ray bursts, optical transients, or neutrino events. (This last test is for information only, as a genuine GW event might or might not be accompanied by other signals.)

As mentioned in Appendix A, we examine the distribution of triggers after each category of veto is applied. In case there is a statistically significant outlier after only category 1 or after categories 1 and 2 are applied, we carry out a follow-up exercise to see if the veto that eventually rejected the event was rightfully applied. There are two reasons that this could be important. First, a very strong gravitational wave from within the Milky Way could cause an instrumental saturation of the sort that we use as a veto; this kind of problem would be easy to diagnose if it were to occur, since the signal would be strong enough for us to see in the moments leading up to the signal-induced saturation. Second, we want to guard against false dismissal of a candidate by other kinds of vetoes, which can have non-negligible dead time associated with them. Some of our vetoes are associated with recognizable forms of false signals; we check to be sure that a vetoed loud event looks like that kind of false signal, and not like a genuine coalescence signal. In the search described in this paper, there was a single statistically significant outlier in the distribution of events after the application of veto categories 1 and 2. The follow-up exercise confirmed that the category 3 test that vetoed that event was correctly applied.

Before unblinding the data, we discovered an error in the computation of the template metric. This metric is used in the placement of the bank and the coincidence test. The error caused the metric distance between templates to be overestimated for the higher mass signals. This has the effect of causing the template placement algorithm to overcover the higher mass region (i.e. to produce a bank with less than the requested 3% loss in signal-to-noise ratio). This increased the computational cost of the search, but did not significantly reduce the sensitivity. However,

this error also affected the coincidence algorithm by overestimating the distance between triggers for high mass signals. Since the coincidence window was empirically tuned on software injections and time-shifted coincidences, the impact on the sensitivity of the search was not significant. Consequently, the decision was taken to unblind the data using the original, suboptimal analysis in order to begin studying any possible detection candidates and to use this result to compute the upper limit (in the absence of a detection). The decision was also taken to perform a complete reanalysis of the data with the corrected metric to verify the (non)detection statement from the original search. The results of the reanalysis were consistent with the original analysis and did not produce any plausible gravitational-wave signals.

APPENDIX C: EFFECTIVE SNR

For this search we employ the same definition of combined effective SNR as was used in the BNS searches of Ref. [11]. The combined effective SNR is constructed as follows.

The single-detector SNR is produced by matched filtering the data against our templates. The complex output from the matched filter, z, is given by

$$z = 4 \int_0^\infty \frac{\tilde{s}(f)^* \tilde{h}(f)}{S_n(f)} df, \qquad (C1)$$

where $\tilde{s}(f)^*$ is the complex conjugate of the Fourier transform of the data, $\tilde{h}(f)$ is the Fourier transform of the template, and $S_n(f)$ is the power spectral density of the noise in the detector. The template normalization σ is given by

$$\sigma^2 = 4 \int_0^\infty \frac{\tilde{h}(f)^* \tilde{h}(f)}{S_n(f)} df. \qquad (C2)$$

The z and σ are combined to give the single-detector SNR ρ, using

$$\rho = \frac{|z|}{\sigma}. \qquad (C3)$$

From ρ we define the *effective SNR* ρ_{eff} as

$$\rho_{\text{eff}}^2 = \frac{\rho^2}{\sqrt{(\frac{\chi^2}{2p-2})(1 + \frac{\rho^2}{250})}}, \qquad (C4)$$

where p is the number of bins used in the χ^2 test, which is a measure of how much the signal in the data looks like the template we are searching for. In the effective SNR, we normalize the χ^2 by $2p - 2$ since it is the number of degrees of freedom of this test.

We then combine the effective SNRs for the single-detector triggers that form a coincident trigger into the *combined effective SNR* ρ_c for that coincident trigger using

$$\rho_c^2 = \sum_{i=1}^N \rho_{\text{eff},i}^2. \qquad (C5)$$

This definition of the combined effective SNR reduces the apparent significance of non-Gaussian instrumental artifacts since it weights the SNR by the χ^2. This effectively cuts down on outliers from the expected SNR distribution due to Gaussian noise. In addition, we test this definition of the combined effective SNR using software injections and find it does not significantly affect the apparent significance of real signals.

APPENDIX D: FALSE ALARM RATE

Previously [11], we defined the loudest event for the entire parameter space based on the combined effective SNR ρ_c (Appendix C). Since we are searching over a larger portion of parameter space than before, we find that the distribution of combined effective SNR for time-shifted coincident triggers varies significantly over different portions of the parameter space. In general, this seems to be affected by two factors. We see a suppression of the combined effective SNR distributions for time-shifted coincident triggers when looking at triple-coincident triggers compared to double-coincident triggers. Also, we find smaller combined effective SNR distributions for time-shifted coincident triggers in the lower mass regions than in the higher mass regions.

For this search, we have decided to divide the parameter space into regions with similar combined effective SNR distributions for time-shifted coincident triggers. We separate the triggers into different categories, where the categories are defined by the mean template masses of the triggers and trigger types (triple-coincident triggers found in triple-coincident time, double-coincident triggers found in triple-coincident time, and double-coincident triggers found in double-coincident time). The categories for this search are given by the combination of three template mass regions with divisions in chirp mass at $M_c = (3.48, 7.40)M_\odot$ with trigger types given by H1H2L1, H1L1, and H2L1 triggers from H1H2L1 triple-coincident time, H1L1 triggers from H1L1 double-coincident time, and H2L1 triggers from H2L1 double-coincident time.

Within each category, the time-shifted coincident triggers provide an estimate of the FAR for each in-time coincident trigger. When we recombine the categories from the same observation time, the FAR of each trigger then needs to be normalized by the number of trials (i.e. the number of categories). This normalization bestows a FAR of $1/T$ with the meaning that, during the observation time covered by this search (T), there is expected to be a single coincidence trigger due to background with a combined effective SNR at that level.

The IFAR is used as our detection statistic, and in-time coincident triggers with the largest IFAR (across all categories) are our best detection candidates.

APPENDIX E: SIMULATED WAVEFORM INJECTIONS

In order to measure the efficiency of our pipeline for recovering GW signals from CBC, we inject several different PN families of waveforms into the data and check to see the fraction of signals that are recovered. The different waveform families used for injections in this search include GeneratePPN computed to Newtonian order in amplitude and 2PN order in phase using formulas from Ref. [38], EOB computed to Newtonian order in amplitude and 3PN order in phase using formulas from Refs. [39–42], PadéT1 computed to Newtonian order in amplitude and 3.5PN order in phase using formulas from Refs. [43,44], and SpinTaylor computed to Newtonian order in amplitude and 3.5PN order in phase using formulas from Refs. [12] and based upon Refs. [35,38,43,45–49], using code from Ref. [50]. Each of these families except for SpinTaylor ignores the effects of spin on the orbital evolution.

Each of these waveform families is injected from a distribution uniform in sky location (right ascension, declination), uniform in the cosine of the inclination angle (ι), and uniform in polarization azimuthal angle (ψ). Each of these waveform families is injected from a distribution uniform in the total mass of the system. Each of these waveform families is also injected uniform in $\log_{10}D$, where D is the physical distance from the Earth to the source in Mpc. This nonphysical distance distribution was chosen in order to test our pipeline on a large range of signal amplitudes.

For the SpinTaylor waveform family, each of the component objects' spin magnitudes is chosen from a distribution uniform in the unitless spin parameter $\hat{a} \equiv (cS)/(Gm^2)$, ranging from 0 to 1. The component objects' spin orientations relative to the initial orbital angular momentum are chosen from a distribution uniform on a sphere.

APPENDIX F: CHIRP DISTANCE

In the adiabatic regime of binary inspiral, gravitational-wave radiation is modeled accurately. We make use of a variety of approximation techniques [38–40,43,44,46,48,51,52] which rely, to some extent, on the slow motion of the compact objects which make up the binary. We can represent the known waveform by

$$h(t) = \frac{1 \text{ Mpc}}{D_{\text{eff}}} A(t) \cos(\phi(t) - \phi_0), \qquad \text{(F1)}$$

where ϕ_0 is some unknown phase. For this search the functions $A(t)$ and $\phi(t)$ are the Newtonian amplitude and 2PN phase evolution, respectively, which depend on the masses and spins of the binary.

The template matched filtering will identify the masses and coalescence time of the binary but not its physical distance D. The signal amplitude received by the detector depends on the detector response functions F_+ and $F_\times$, and the inclination angle of the source ι, which are unknown. We can only obtain the *effective distance* D_{eff}, which appears in Eq. (F1) defined as [22]

$$D_{\text{eff}} = \frac{D}{\sqrt{F_+^2 (1 + \cos^2\iota)^2/4 + F_\times^2 (\cos\iota)^2}}. \qquad \text{(F2)}$$

The effective distance of a binary may be larger than its physical distance.

Since the amplitude of a gravitational wave scales as the chirp mass M_c to the five-sixths power, it is convenient to normalize the effective distance by this, obtaining the *chirp distance*, which is given by

$$D_{\text{chirp}} = D_{\text{eff}} \left(\frac{M_{c,\text{BNS}}}{M_c}\right)^{5/6}, \qquad \text{(F3)}$$

where $M_{c,\text{BNS}}$ is the chirp mass of a canonical BNS system. This distance is useful in evaluating the efficiency of the search as a function of distance since the efficiency will then be approximately independent of mass.

APPENDIX G: POSTERIOR AND UPPER LIMIT CALCULATION

Calculating an upper limit on the rate of coalescences in the loudest-event formalism requires knowledge of the cumulative luminosity to which the search is sensitive and a measure of the likelihood that the loudest event was due to the observed background. The cumulative luminosity quantifies the potential sources of observable CBC, as measured by blue-light luminosity of the galaxies, which can be detected by our search. It is calculated by multiplying the efficiency of signal recovery for the search as a function of distance by the physical luminosity as a function of distance and integrating their product over distance. We combine these with the time analyzed to calculate the posterior on the rate for the search. This is, assuming a uniform prior on the rate, given by [33]

$$p(\mu | \mathcal{C}_L, T, \Lambda) = \frac{\mathcal{C}_L T}{1 + \Lambda} (1 + \mu \mathcal{C}_L T \Lambda) e^{-\mu \mathcal{C}_L T}, \qquad \text{(G1)}$$

where μ is the rate, $\mathcal{C}_L$ is the cumulative luminosity, T is the analyzed time, and Λ is a measure of the likelihood of detecting a single event with loudness parameter x versus such an event occurring due to the experimental background, given by [33]

$$\Lambda(x) = \left(\frac{-1}{\mathcal{C}_L} \frac{d\mathcal{C}_L}{dx}\right) \left(\frac{1}{P_0} \frac{dP_0}{dx}\right)^{-1}. \qquad \text{(G2)}$$

The posterior (G1) assumes a known value of $\mathcal{C}_L$ associated with the search. In reality, $\mathcal{C}_L$ is associated with systematic uncertainties, which we model as unknown multiplicative factors, each log-normally distributed about 1 with errors described in Appendix H. The widths of those distributions are given in Table I. Marginalizing over all of

those unknown factors, and thus over $\mathcal{C}_L$, gives a marginalized posterior:

$$p(\mu|T, \Lambda) = \int p_d(\mathcal{C}_L) p(\mu|\mathcal{C}_L, T, \Lambda) d\mathcal{C}_L, \qquad \text{(G3)}$$

where $p_d(\mathcal{C}_L)$ is the combined probability distribution function for $\mathcal{C}_L$, given all of those unknown factors.

The results of several experiments (e.g. different types of S5 observing time and previous runs such as S3 and S4) can be combined by taking the product of their likelihood functions; in the case of uniform priors, this is equivalent to taking the product of their posteriors, allowing us to define the upper limit on the rate μ at a confidence level α by solving

$$\alpha = \int_0^\mu \prod_i p_i(\mu') d\mu', \qquad \text{(G4)}$$

where the $p_i(\mu')$ are the marginalized posteriors from different experiments calculated using a uniform prior on the rate.

APPENDIX H: SYSTEMATIC ERROR CALCULATION

Systematic errors associated with CBC searches for GW signals include errors associated with detector calibrations, simulation waveforms, Monte Carlo statistics, and galaxy catalog distances and magnitudes. Calculating these errors in terms of the cumulative luminosity is described below [19].

We refer to statistical errors associated with the efficiency calculation as *Monte Carlo errors*. Since we calculate the efficiency as a function of distance, we calculate the error for a particular distance bin using the binomial formula, which gives an error of zero when the efficiency is zero or one, or when there are no injections in that bin. This error is then multiplied by the physical luminosity as a function of distance and integrated over distance to get the Monte Carlo error in units of luminosity.

Calibration errors in the detectors are errors on the amplitude of the noise floor. These errors affect the amplitude, and in turn the distance, at which we made injections to calculate the efficiency of our search, since we made the injections assuming a specific value of the noise floor. The one-sigma uncertainty in the amplitude (and thus the distance) associated with the calibration was 8.1% for H1, 7.2% for H2, and 6.0% for L1. We use these numbers to calculate the calibration error given in Table I in units of luminosity by combining the logarithmic errors in quadrature.

Waveform errors are associated with how different the true signals are from what we use to measure the efficiency of our pipeline (i.e. the mismatch between the true signals and our injections). This error effectively reduces the distances in our efficiency calculation since we do not recover all of the power available in the signal due to the mismatch between the signal and our injections. We calculate the waveform error in units of luminosity assuming a waveform mismatch of 10% [43,53].

Galaxy errors are errors associated with our galaxy catalog [1] used to construct the physical luminosity. Galaxy errors come in two types: *distance errors* and *magnitude errors*. To calculate the error on the luminosity due to distance errors, the physical luminosity calculation is modified such that the galaxies' distances are increased by a factor $1 + \kappa_j$, where κ_j is the uncertainty in the jth galaxy's distance given in the galaxy catalog. The galaxies' luminosities are also increased by a factor $(1 + \kappa_j)^2$ since these luminosities are only known in terms of the galaxies' magnitude and distance. To calculate the error on the luminosity due to magnitude errors, the physical luminosity calculation is changed such that the galaxies' luminosities are increased by an amount associated with the magnitude errors given in the galaxy catalog.

APPENDIX I: SPINNING SEARCH COMPARISON

The SPA template waveforms used in this search and described in this paper do not take spin into account. A phenomenological template family to search for spinning black hole and neutron star binaries was developed in [12], referred to as *BCVSpin*, and has been used in a search of S3 data [13]. Using both of these template banks to compute the efficiency of recovering signals from spinning waveforms for the different search methods, we find that for a comparable number of false alarms, SPA and BCVSpin have approximately the same efficiencies, implying it is not necessary to perform a search using BCVSpin templates in order to target spinning signals. The comparison of searches for spinning binaries using different signal models and template banks is discussed further in Ref. [31].

What is important for a search is how efficient banks are in picking up signals in the data. Given a large number of injections in the data, the efficiency is the ratio of the number of found injections to the total number of injections made. A fair comparison requires that efficiencies be evaluated *for the same FAR*. To estimate the background rate, we counted the number of coincident triggers in time-shifted data between H1 and L1.

The SNR for BCVSpin involves 6 degrees of freedom, compared to only 2 for SPA. As a consequence, BCVSpin picks up glitches more easily, and to have the same background rate as for SPA, it needs a higher SNR threshold. (This problem had already been pointed out and discussed in [12]; here we are seeing it in real data.) It was found that SPA with a SNR threshold of 5.5 and BCVSpin with a SNR threshold of 8 lead to comparable FARs (Fig. 4).

With these SNR thresholds, we are in a position to compare the efficiencies of SPA and BCVSpin banks for a given FAR. For our purposes, an injection will be considered found if it had a SNR above the chosen threshold
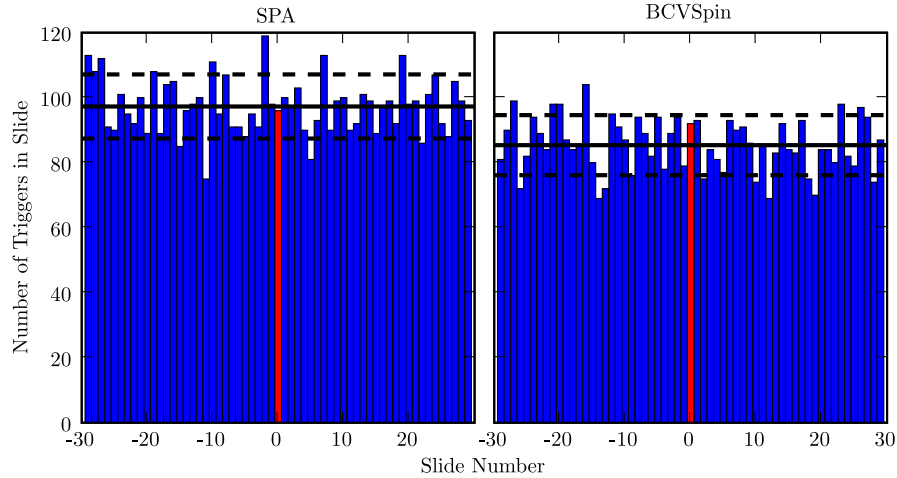
FIG. 4 (color online).   Histograms of the number of time-shifted coincident triggers for SPA (left panel) and BCVSpin (right panel) templates, in about 9 days of playground data from H1 and L1. In this investigation, we applied a SNR threshold of 5.5 for SPA and 8 for BCVSpin; the number of triggers is approximately the same in the two cases.
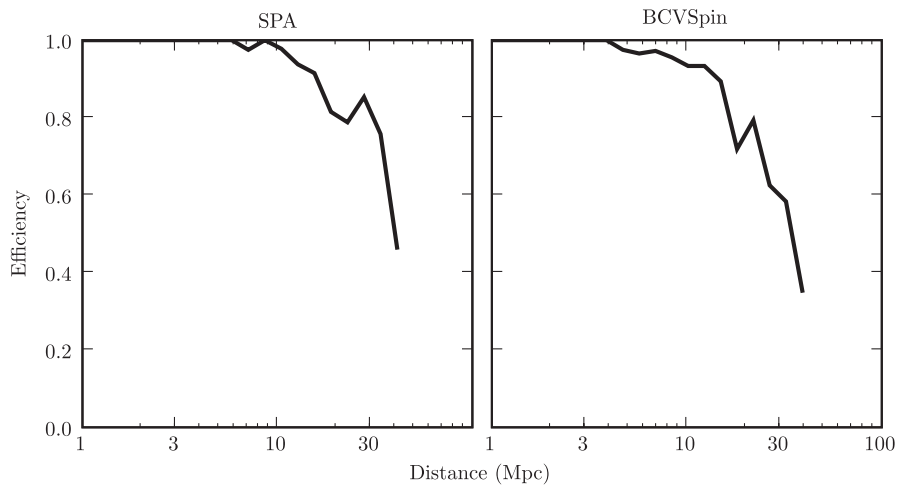

FIG. 5.   Injection recovery efficiencies plotted against distance for SPA (left panel) and BCVSpin (right panel) templates.

with at least one template in the bank, within a certain time interval around the time when the injection was actually made. In the case of SPA, the width of this interval can be chosen to be 40 ms. BCVSpin templates, being phenomenological, turn out to have a larger timing inaccuracy, and an interval of 100 ms was found to be more appropriate. We made 1128 injections distributed logarithmically in distance between 1 Mpc and 50 Mpc, with component masses randomly chosen between $1M_\odot$ and $30M_\odot$ but restricting total mass to $30M_\odot$, component spin magnitudes

$0.7 < \hat{a}_i < 1$, $i = 1$, 2, and arbitrary directions for the initial spin vectors. For the SNR thresholds of 5.5 for SPA and 8 for BCVSpin, in H1 the efficiency of SPA came out to be 0.93, versus 0.89 for BCVSpin; for L1 the numbers are similar. Figure 5 shows the efficiencies binned in distance. Hence, for comparable FARs, SPA and BCVSpin have approximately the same efficiencies, showing it is not necessary to perform a search using BCVSpin templates in order to target spinning signals.

[1] R. K. Kopparapu, C. Hanna, V. Kalogera, R. O'Shaughnessy, G. Gonzalez, P. R. Brady, and S. Fairhurst, Astrophys. J. **675**, 1459 (2008).

[2] V. Kalogera, R. Narayan, D. N. Spergel, and J. H. Taylor, Astrophys. J. **556**, 340 (2001).

[3] V. Kalogera, C. Kim, D. R. Lorimer, M. Burgay, N. D'Amico, A. Possenti, R. N. Manchester, A. G. Lyne, B. C. Joshi, M. A. McLaughlin, *et al.*, Astrophys. J. **601**, L179 (2004); **614**, L137(E) (2004).

[4] V. Kalogera *et al.*, Astrophys. J. Lett. **614**, L137 (2004).

[5] R. O'Shaughnessy, C. Kim, V. Kalogera, and K. Belczynski, Astrophys. J. **672**, 479 (2008).

[6] R. O'Shaughnessy, C. Kim, T. Fragos, V. Kalogera, and K. Belczynski, Astrophys. J. **633**, 1076 (2005).

[7] B. Abbott *et al.* (LIGO Scientific Collaboration), Phys. Rev. D **69**, 122001 (2004).

[8] B. Abbott *et al.* (LIGO Scientific Collaboration), Phys. Rev. D **72**, 082001 (2005).

[9] B. Abbott *et al.* (LIGO Scientific Collaboration), Phys. Rev. D **72**, 082002 (2005).

[10] B. Abbott *et al.* (LIGO Scientific Collaboration), Phys. Rev. D **73**, 062001 (2006).

[11] B. Abbott *et al.* (LIGO Scientific Collaboration), Phys. Rev. D **77**, 062002 (2008).

[12] A. Buonanno, Y. Chen, and M. Vallisneri, Phys. Rev. D **67**, 104025 (2003); **74**, 029904(E) (2006).

[13] B. Abbott *et al.* (LIGO Scientific Collaboration), Phys. Rev. D **78**, 042002 (2008).

[14] Y. Pan, A. Buonanno, Y.-b. Chen, and M. Vallisneri, Phys. Rev. D **69**, 104017 (2004); **74**, 029905(E) (2006).

[15] A. Buonanno, Y.-b. Chen, Y. Pan, and M. Vallisneri, Phys. Rev. D **70**, 104003 (2004); **74**, 029902(E) (2006).

[16] A. Buonanno, Y. Chen, Y. Pan, H. Tagoshi, and M. Vallisneri, Phys. Rev. D **72**, 084027 (2005).

[17] B. A. Allen, W. G. Anderson, P. R. Brady, D. A. Brown, and J. D. E. Creighton, arXiv:gr-qc/0509116.

[18] LIGO Scientific Collaboration, LIGO Technical Report No. LIGO-T070109-01, 2007, http://www.ligo.caltech.edu/docs/T/T070109-01.pdf.

[19] P. R. Brady and S. Fairhurst, Classical Quantum Gravity **25**, 105002 (2008).

[20] S. Babak, Balasubramanian, D. Churches, T. Cokelaer, and B. Sathyaprakash, Classical Quantum Gravity **23**, 5477 (2006).

[21] B. Allen, Phys. Rev. D **71**, 062001 (2005).

[22] K. S. Thorne, in *Three Hundred Years of Gravitation*, edited by S. W. Hawking and W. Israel (Cambridge University Press, Cambridge, England, 1987), Chap. 9, p. 330.

[23] B. S. Sathyaprakash and S. V. Dhurandhar, Phys. Rev. D **44**, 3819 (1991).

[24] S. Droz, D. J. Knapp, E. Poisson, and B. J. Owen, Phys. Rev. D **59**, 124016 (1999).

[25] T. Cokelaer, Phys. Rev. D **76**, 102004 (2007).

[26] C. A. K. Robinson, B. S. Sathyaprakash, and A. S. Sengupta, Phys. Rev. D **78**, 062002 (2008).

[27] R. Balasubramanian, B. S. Sathyaprakash, and S. V. Dhurandhar, Phys. Rev. D **53**, 3033 (1996).

[28] B. J. Owen, Phys. Rev. D **53**, 6749 (1996).

[29] B. J. Owen and B. S. Sathyaprakash, Phys. Rev. D **60**, 022002 (1999).

[30] A. S. Sengupta, J. A. Gupchup, and C. A. K. Robinson (unpublished).

[31] C. Van Den Broeck, D. A. Brown, T. Cokelaer, I. Harry, G. Jones, B. S. Sathyaprakash, H. Tagoshi, and H. Takahashi (unpublished).

[32] P. R. Brady, J. D. E. Creighton, and A. G. Wiseman, Classical Quantum Gravity **21**, S1775 (2004).

[33] R. Biswas, P. R. Brady, J. D. E. Creighton, and S. Fairhurst, arXiv:0710.0465.

[34] R. N. Manchester, G. B. Hobbs, A. Teoh, and M. Hobbs, Astron. J. **129**, 1993 (2005).

[35] T. A. Apostolatos, C. Cutler, G. J. Sussman, and K. S. Thorne, Phys. Rev. D **49**, 6274 (1994).

[36] R. O'Shaughnessy, C. Kim, V. Kalogera, and K. Belczynski, Astrophys. J. **672**, 479 (2008).

[37] R. Gouaty and the LIGO Scientific Collaboration, Classical Quantum Gravity **25**, 184006 (2008).

[38] L. Blanchet, B. R. Iyer, C. M. Will, and A. G. Wiseman, Classical Quantum Gravity **13**, 575 (1996).

[39] A. Buonanno and T. Damour, Phys. Rev. D **59**, 084006 (1999).

[40] A. Buonanno and T. Damour, Phys. Rev. D **62**, 064015 (2000).

[41] T. Damour, P. Jaranowski, and G. Schäfer, Phys. Rev. D **62**, 084011 (2000).

[42] T. Damour, Phys. Rev. D **64**, 124013 (2001).

[43] T. Damour, B. R. Iyer, and B. S. Sathyaprakash, Phys. Rev. D **63**, 044023 (2001).

[44] T. Damour, B. R. Iyer, and B. S. Sathyaprakash, Phys. Rev. D **57**, 885 (1998).

[45] L. E. Kidder, Phys. Rev. D **52**, 821 (1995).

[46] L. Blanchet, T. Damour, B. R. Iyer, C. M. Will, and A. G. Wiseman, Phys. Rev. Lett. **74**, 3515 (1995).

[47] L. Blanchet, Phys. Rev. D **54**, 1417 (1996).

[48] L. Blanchet, G. Faye, B. R. Iyer, and B. Joguet, Phys. Rev. D **65**, 061501(R) (2002).

[49] L. E. Kidder, C. M. Will, and A. G. Wiseman, Phys. Rev. D **47**, R4183 (1993).

[50] LSC Algorithm Library software packages LAL, LALWRAPPER, and LALAPPS (http://www.lsc-group.phys.uwm.edu/lal).

[51] L. Blanchet, T. Damour, and B. R. Iyer, Phys. Rev. D **51**, 5360 (1995).

[52] L. Blanchet, T. Damour, G. Esposito-Farèse, and B. R. Iyer, Phys. Rev. Lett. **93**, 091101 (2004).

[53] Y. Pan *et al.*, Phys. Rev. D **77**, 024014 (2008).